Journal of Environmental Chemical Engineering 10 (2022) 107282

Contents lists available at ScienceDirect

Journal of Environmental Chemical Engineering

journal homepage: www.elsevier.com/locate/jece

Confined space synthesis of chromium–based metal–organic frameworks in activated carbon: Synergistic effect on the adsorption of contaminants of emerging concern from water

Juan C. Muñoz-Senmache [a], Perla E. Cruz-Tato [b], Eduardo Nicolau [b], Arturo J. Hernández-Maldonado [a,*]

[a] Department of Chemical Engineering, University of Puerto Rico, Mayagüez Campus, Mayagüez, Puerto Rico 00681-9000, USA
[b] Department of Chemistry, University of Puerto Rico, Rio Piedras Campus, San Juan, Puerto Rico 00925, USA

ARTICLE INFO

Editor: Dong-Yeun Ko

Keywords:
Metal-organic frameworks
Confined space synthesis
Contaminants of emerging concern
Adsorption
Water treatment

ABSTRACT

The steadfast presence of contaminants of emerging concern (CECs) in the environment calls for tailored remediation strategies. In this regard, Cr-based metal-organic frameworks (MOFs; MIL-100Cr and MIL-101Cr) were grown inside of activated carbon (AC) pores via confined synthesis for a superior adsorptive removal of those CECs from water. The composites CMOF-100Cr and CMOF-101Cr, as well as the apohost AC and pure MOFs, were characterized via X-ray diffraction (XRD), scanning electron microscopy (SEM), energy dispersive analysis by X-rays (EDAX), nitrogen adsorption–desorption, thermogravimetric analysis (TGA), X-ray photoelectron spectroscopy, and zeta potential measurements. XRD, SEM/EDAX, TGA, and pore size distribution data provided direct evidence of the successfully confined space syntheses of the hierarchical composites. Occupancy of the large voids of AC by the MOF was 100% and 43% for CMOF-100Cr and CMOF-101Cr, respectively. The adsorption capacity of the materials was evaluated in both single- and multi-component fashion at neutral pH and low CEC concentrations (μg L^{-1}). The CECs were caffeine (CFN), carbamazepine (CBZ), clofibric acid (CA), naproxen (NPX), and metabolites 10,11-epoxycarbamazepine (Ep-CBZ), *o*-desmethylnaproxen (*o*-DMN), paraxanthine (PXN), and salicylic acid (SA). In general, the observed capacities for both single and multi-component adsorption of CECs increased as follows MIL-100Cr < < MIL-101Cr < CMOF-101Cr < AC < < CMOF-100Cr. Compared to the composite containing MIL-100Fe (i.e., CMOF-100Fe) previously developed by our group, the substitution of the metal node by Cr^{3+} produced significant enhancements in CEC uptake capacities. The affinity of CMOF-100Cr toward CECs increases as follow: SA < CA< *o*-DMN < NPX < PXN < CFN < Ep-CBZ < CBZ.
Environmental significance: The persistence of contaminants of emerging concern (CECs) in water mandates the development of tailored remediation strategies. To be suitable, these must consider efficacy and avoid undesired byproducts. An attempt to individually grow two chromium-based nanoporous metal-organic frameworks, each possessing particular linkers, within the pores of an activated carbon via confined space synthesis has proven to be effective in the adsorptive removal of a set of CECs that included metabolites. Furthermore, the adsorption was conducted in both single- and multi-component fashion to gain insight into the CECs competitive nature during uptake. The hierarchical composite adsorbents exhibited superior uptake capacity because of the synergistic combination of hydrophobicity and specific interactions between the metal node and the CECs, while multiple adsorption cycles were possible via thermal regeneration.

1. Introduction

For more than two decades, the presence of contaminants of emerging concern (CECs) in sources of water has attracted attention from the scientific community due to their inherent capability to produce an undesirable biological effect on living organisms and the overall impact on the environment, even at very low doses [1–7]. Effective remediation of CECs also remains a challenge, even with current improvements in the capacity of water treatment (WT) operations to mitigate pathways associated with the exposition to humans, animals,

* Corresponding author.
E-mail address: arturoj.hernandez@upr.edu (A.J. Hernández-Maldonado).

https://doi.org/10.1016/j.jece.2022.107282
Received 2 November 2021; Received in revised form 18 January 2022; Accepted 24 January 2022
Available online 29 January 2022

and edible plants [2,4,8–11]. Therefore, there are significant opportunities in diverse WT areas to enable CEC remediation technologies that would allow for the attainment of higher clean water standards and to prevent further potential environmental impact, especially if policies for the use of reclaimed water are expected to be recurrent.

In most cases, the concentrations of CECs in water remain at ng L^{-1}-μg L^{-1} levels, and removal is usually left to the tertiary stage processes within WTs. Among these, adsorption with porous materials is an attractive remediation option. Positive features include the possibility of using bottom-up designed adsorbent materials, with surfaces tailored to selectively target CECs, the non-generation of toxic or unknown toxicity subproducts during the uptake of CECs, and the possibility to achieve multi-cycle operations via on-site regeneration [12–17]. Metal-organic frameworks (MOFs) have shown promising performance toward the uptake at CECs, particularly because of the potential for surface tailoring [9,15,18–20]. MOFs are crystalline materials built by stable self-assembly between metal nodes and organic ligands resulting in 3D structures with well-defined pores. The tunable structure of MOFs, large surface area, as well as the high content of active, exposed metal adsorption sites have already shown that these materials are suitable for a wide variety of tasks such as water remediation, gas separations, catalysis and photocatalysis, electronic sensors, supercapacitors, and highly sensitive chemical detection [9,15,18–33].

Chromium-based MOF structures MIL-100(Cr) or MIL-101(Cr) (MIL stands for Matériaux de l'Institut Lavoisier) are hydrothermally stable materials and, in general, suitable for the uptake of contaminants from water [34]. These MIL series MOFs are constituted by oxo-centered trimers of Cr^{3+} octahedra linked by 1,3,5-benzene tricarboxylic acid for the MIL-100 series and 1,4-benzene dicarboxylic acid for the MIL-101 [35]. The resulting structures show a zeolitic architecture, containing micro/mesoporous cages of 24 and 29 Å for MIL-100 and 29 and 34 Å for MIL-101, which are accessible through pore windows of 5 and 9 Å, and 12 and 15 Å, respectively. These frameworks also contain high concentrations of chemically tunable unsaturated metal sites [36] which offer potential adsorption sites for the capture of organic pollutants (i.e., CECs) via interactions that include π-π complexation (see Scheme 1). Although MIL-100Cr is an isoreticular assembly of MIL-100Fe, different interaction levels toward specific CECs can be accomplished via the choice of the transition metal core or node. Likewise, the substituents of the organic linker (two carboxyl groups for MIL-101 and three carboxyl groups for MIL-100 structure) have a strong influence on the structural conformation of the MOF and therefore adsorbate-adsorbent interactions. Despite the elevated qualities of these adsorbents to potentially carry-out the efficient capture of CECs at concentrations typically observed in the environment (i.e., ng L^{-1} – mg L^{-1}), MOF-based adsorbents must also possess the ability to provide adequate driven forces to achieve the desired selectivity. Previous efforts found that preparation of zeolitic-based composites via confined space synthesis to synergistically achieve hydrophobicity and high chemical functionality density (i.e., transition metal content) are crucial characteristics to achieve high CEC uptakes from water [20,37–40]. Indeed, it can be hypothesized that a hierarchical composite materials based on the confined space synthesis of a crystalline material (i.e., MOFs) inside of the pores of activated carbon (AC) take advantage of the high hydrophobic character from the latter and the chemical capabilities from the former (see Scheme 1) [41]. Particularly, this core/shell arrangement has high relevance for water remediation applications since the confining material (i.e., AC) provides not just hydrophobic interactions toward organic pollutants but also an effective barrier to diminish water competition for active adsorption sites. This could have a tremendous impact on the uptake capacity toward CECs since specific interactions such as π-complexation or π-π stacking between adsorbates and the confined phase of the composite adsorbent (i.e., MOF) can be favorably exploited (see Scheme 1). This would be advantageous to treat CEC contaminants that appear in water sources at very concentration levels (i.e., ng L^{-1}-μg L^{-1}) since the overall adsorption surface potential will probably include the addition of contributions beyond non-specific ones (i.e., just electrostatic based).

The main goal of this work is the preparation of two hierarchical composite adsorbents based on the confined space synthesis of MIL-100Cr and MIL-101Cr structures within an activated carbon pore, to limit the hydrophilicity of the corresponding MOF phase, and synergistically increase the capacity toward the uptake of selected CECs depending on the MOF organic linker being employed (dicarboxylic or tricarboxylic acid, see Scheme 1.) The choice of organic linker will impart different metal-organic coordination environments as mentioned above, and hence generate unique surface and textural characteristics. All of the adsorbent materials were fully characterized to check for long-range order, thermal stability, textural properties, and hydrophobicity. The CEC chosen as adsorbates are not only known to be of considerable occurrence in the environment but also exhibit a considerable range of molecular structure and physio-chemical properties (see Table S1). These include carbamazepine (CBZ), caffeine (CFN), naproxen (NPX), clofibric acid (CA), and metabolites such as salicylic acid (SA), 10,11-epoxycarbamazepine (Ep-CBZ), paraxanthine (PXN), and *o*-desmethylnaproxen (o-DMN). The latter three result from the partial decomposition of primary molecules CBZ, CFN, and NPX, respectively. The uptake tests were conducted in both single and multi-component fashion and for very diluted concentrations of CECs to match levels currently observed in the environment. Surface spectroscopy and zeta potential, along with the CEC adsorption observations, were used in an attempt to elucidate some of the underlying uptake mechanisms. Furthermore, the composite that exhibited the overall superior adsorption performance was tested for thermal regeneration through multiple cycles.

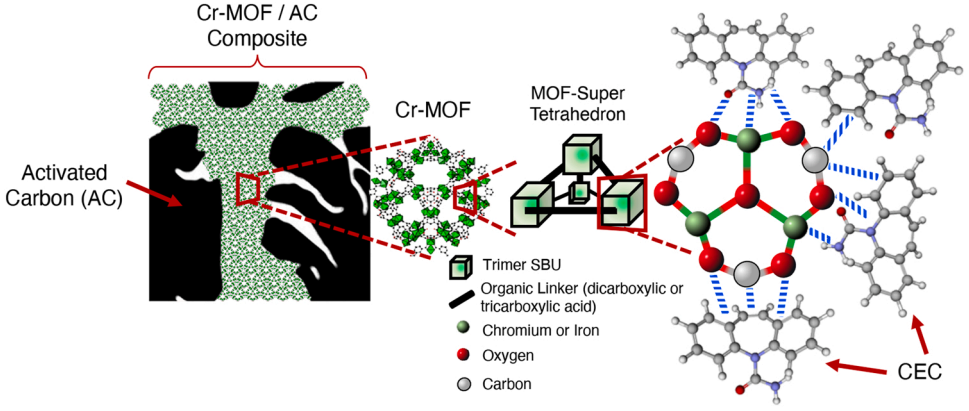

Scheme 1. Hierarchical MOF/AC composite (CMOF) assembly for CEC adsorption from water. MOF phase organic linker is either a di- or tri-carboxylic moiety and the node is Cr^{3+}.

2. Experimental section

2.1. Reagents and materials

The following reagents were acquired from Sigma-Aldrich and used as received: metallic chromium powder, benzene 1,3,5- tricarboxylic acid (H_3BTC), hydrofluoric acid (HF, 48% wt.), ammonium fluoride (NH_4F), and anhydrous ethanol (EtOH) were used to synthesize MIL-100Cr and CMOF-100Cr. To synthesize MIL-101Cr and CMOF-101Cr, chromium nitrate nonahydrate, benzene 1,4- dicarboxylic acid (H_2BDC), HF, EtOH, and N,N- dimethylformamide (DMF) were employed. Activated carbon (Darko KB-G) was used to synthesize both CMOF-100Cr and CMOF-101Cr hierarchical composites. The water used during syntheses was both distilled/deionized (DI).

For the CEC adsorption experiments, the following reagents were purchased from Sigma-Aldrich and also used as received: caffeine (CFN), carbamazepine (CBZ), clofibric acid (CA), 10,11-epoxycarbamazepine or 10,11-carbamazepine epoxide (Ep-CBZ), naproxen (NPX), *o*-desmethylnaproxen (*o*-DMN), paraxanthine (PXN) and salicylic acid (SA), The solvents used for the chromatography–mass spectroscopy analyses were acetonitrile, water, ammonium acetate, and formic acid (all LC-MS grade) and were obtained from Honeywell (USA) and Agilent Technologies (USA).

All the gases used for thermal gravimetric analyses, regeneration tests, and the nitrogen volumetric gas adsorption tests used to elucidate textural properties of the adsorbents were of ultrahigh purity grade (Praxair, USA).

2.2. Synthesis of MIL-100Cr and MIL-100Cr/Activated carbon (CMOF-100Cr) composite

The MOF material was synthesized based on procedures reported elsewhere [35,42] with some modifications. A typical synthesis contained 1.0 Cr: 0.67 H_3BTC: 2.0 HF: 265.0 H_2O. The metallic chromium was dissolved in an aqueous solution of HF using a Teflon beaker, then H_3BTC was added to the mixture and transferred to a 50 mL Teflon lined reactor and placed in a force convection oven. To avoid the formation of the MIL-96(Cr) phase, and to compensate for heat convection losses, the oven was set to a ramp and soak program as follows: heating from ambient at 23 °C h^{-1} until the 235 °C mark, and soaking at that temperature for 90 h, followed by cooling to room temperature also at 23 °C h^{-1}. The resulting, green-colored MOF powder was recovered using vacuum-assisted filtration and washed under reflux with ethanol at 65 °C for 4 h and water at 90 °C for 4 h. Finally, the solids were recovered and dried overnight at 100 °C.

The synthesis of the MIL-100Cr/activated carbon composite material (CMOF-100Cr) was developed based on a procedure described elsewhere [38]. It consists of a dual-stage approach: (1) dispersion of the organic ligand (i.e., H_3BTC) onto AC followed by (2) addition of Cr, HF, and H_2O and complete reaction using the MOF procedure shown above. The amounts of AC and H_3BTC used to make the dispersion were estimated based on the synthesis yield of MIL-100Cr (1 g of H_3BTC in 10 g of EtOH, and 1.47 g of AC in 10 mL of ligand's solution). Also, the dispersion was performed by mixing the AC and ligand solution, and then stirring vigorously for 24 h at room temperature. Then the ethanol contained in the mixture was evaporated in a forced convection oven at 90 °C for 24 h.

2.3. Synthesis of MIL-101(Cr) and MIL-101Cr/Activated carbon (CMOF-101Cr) composite

The synthesis of MIL-101Cr was made following procedures found elsewhere [43,44]. Briefly, 1.0 $Cr_3(NO_3)_3.9\ H_2O$: 1.0 H_2BDC: 1.0 HF: 265.0 H_2O were mixed in a Teflon-lined autoclave reactor and placed in a preheated convection oven at 220 °C. After 8 h, the reactor was naturally cooled down to room temperature, and the also green-colored solids were recovered via vacuum-assisted filtration. The removal of non-reactant chemicals was carried out using washing stages under reflux of DMF at 140 °C for 4 h, EtOH at 65 °C for 6 h., NH_4F solution, and hot water. The solids were recovered and dried overnight at 100 °C.

The synthesis of the composite MIL-101Cr/activated carbon (CMOF-101Cr) was based on similar conditions as those used for the corresponding pure MOF phase synthesis. However, the Cr: H_2BDC molar ratio was modified to avoid the formation of undesired amorphous phases within the composite material. The procedure used was as follows: 1 g of organic ligand (i.e., H_2BDC) was dissolved in 16 mL of DMF, then 0.84 g of AC was added to the solution, and the mixture was vigorously stirred for 24 h at room temperature. Then, the AC/ligands solution was placed inside a forced convection oven at 155 °C for 3 h and later placed in a vacuum oven at 155 °C for 21 h. The metal node powder was dissolved in a solution of 0.3 mL of HF 48% and 30 mL of DI water and added to the dried AC/ligand mixture. The resulting mixture was then transferred to a Teflon-lined reactor, sealed, and placed in a preheated forced convection oven at 220 °C for 8 h, and then cooled down until room temperature. Finally, the resulting solids were recovered via vacuum-assisted filtration and the removal of the unreacted reagents was done following the same procedure used for the MIL-101Cr synthesis.

2.4. Materials characterization

The long-range order of the crystalline phases was verified by means of powder X-ray diffraction (XRD). The equipment used to collect the patterns was a Rigaku Ultima III unit fitted with a Cu anode ($\lambda = 1.5418$ Å) operated at 40 kV and 44 mA. The XRD patterns were gathered at a scanning speed of 0.5° min^{-1} and 2θ range from 2° to 20°. Particle morphology and elemental composition were assessed via scanning electron microscopy (SEM) using a JEOL JSM-6480LV unit fitted with an energy-dispersive analysis by X-ray (EDAX) system. Prior to the analysis, the samples were sputtered with gold, ca. 10 nm. Meanwhile, hydrophobicity of the materials was assessed via water contact angle measurements, which were performed using a Kruss DSA – 25B contact angle meter fitted with a high-resolution/high-speed camera.

Thermogravimetric analyses (TGA) were used to verify the thermal stability of the materials and also to elucidate the thermal decomposition mechanism of the materials. The experiments were conducted in a D550 TGA TA Instruments equipment operated with a constant flow of nitrogen (60 mL min^{-1}) as carrier gas. The materials were each heated at 10 °C min^{-1} from room temperature up to 600 °C. Prior to the analysis, 10 mg of each material were exposed to environmental humidity (HR ~60%) for 30 min to achieve appropriate baseline comparisons.

Estimation of the textural properties was done using equilibrium nitrogen adsorption–desorption data. The isotherms were collected at −196 °C using a Micromeritics ASAP 2020 volumetric adsorption instrument fitted with turbomolecular drag pumps. Prior to each measurement, the materials were outgassed at 120 °C for 12 h while AC and CMOF's were outgassed at 150 °C for 16 h. The surface area values were estimated using the BET (Brunauer, Emmett, and Teller) isotherm model [45]. Pore size distributions (PSDs) were gathered combining a Barrett – Joyner – Halenda [46] (BJH) model to estimate the mesopore portion and the Horvath – Kawazoe approach with the Cheng-Yang correction (HK-CY) [47] to determine the micropore portion.

Relevant chemical states present in the adsorbents were determined via X-ray photoelectron spectroscopy (XPS). These tests were conducted using a PHI Versa Probe (II) equipped with monochromatized Al Kα radiation ($h\nu = 1486.6$ eV). The high-resolution elemental spectra were gathered using a pass energy of 46.95 eV at 0.1 eV steps and calibrated using C 1 s (284.5 eV). Prior to the measurements, the materials were outgassed overnight at room temperature inside the intro vacuum chamber. Additionally, CMOF-100Cr containing adsorbed CBZ was analyzed to elucidate the interactions between the adsorbent and the

adsorbate. The spent CMOF-100Cr material was recovered via centrifugation and dried overnight at 90 °C.

To estimate the overall surface charge profile of the materials as a function of pH, zeta potential measurements were developed using a ZetaPals equipment from Brookhaven Instruments and fitted with an auto-titration system. For a typical test, 1 mg of each adsorbent was suspended in an aqueous solution of 1 mM of KNO_3, and solutions of HNO_3 and KOH were used to vary the pH during the measurements.

2.5. CEC adsorption experiments

A transient profile for CBZ uptake onto MIL-100Cr or CMOF-100Cr was recorded to elucidate the time required to achieve equilibrium conditions and estimate a diffusion coefficient. The CBZ/MIL-100Cr or CBZ/CMOF-100Cr pairs were chosen among the other variants due to the particular combination of the physio-chemical properties of CBZ (i.e., dimensions and pKa) and the effective pore dimensions of the said MOF or composite. This combination should offer the most significant resistance to the transport of a bulky and rather neutral CEC through a material with micropores. The transient experiment involved using 10 mL of a stock solution of CBZ at 200 μg L^{-1}; the test was performed in triplicate fashion, with 10 mg of adsorbent and borosilicate centrifugate tubes while shaking at 250 rpm at room temperature for predetermined periods. The tubes and contents were centrifuged at 8500 rpm for at least 5 min, and samples were taken from the supernatant and filtered using 0.2 μm PTFE discs and transferred to 2.5 mL amber glass vials. The treated aqueous phases were then analyzed using an Agilent 1290 high-performance liquid chromatography system (HPLC) fitted with an Agilent Zorbax Eclipse Plus C18 column (2.1 mm × 50 mm and particle size 1.8 mm) operated at 40 °C. Ultrapure water and acetonitrile were used as mobile phases at 0.4 mL min^{-1}. The HPLC system was coupled to a 6460 triple quadrupole mass spectrometer (HPLC-MS/MS) with an Agilent Jet Stream electrospray ionization (AJS-ESI) system with multiple reaction monitoring (MRM). The resulting concentration of the samples after the adsorption process were calculated by direct comparison with a calibration curve, while the adsorbed amount of the CEC was estimated via a mass balance:

$$q(t) = \frac{[C_0 - C(t)]V_{solution}}{V_{adsrbent}} \quad (1)$$

where $q(t)$ is the adsorbed amount, expressed in μg cm^{-3}, C_O and $C(t)$ are the initial and transient concentration of the CEC in the solution, respectively, both expressed in μg L^{-1}, $V_{solution}$ (L) is the volume of the CEC aqueous solution, and the $V_{adsorbent}$ is the solid volume of the adsorbent (cm^{-3}). Fractional uptake profiles were constructed by dividing the observed transient adsorbed amount $q(t)$ by the corresponding amounts when a steady state is reached and then plotting the resulting values versus time. These fractional uptake profiles were then fitted with a phenomenological transport model to estimate diffusivity values. The model assumes that the greatest resistance to transport of the CECs lies on the pores (e.g., microporosity) of the adsorbent and that the particles approach spheres. Details of this model are available elsewhere [38,48].

For batch CEC equilibrium adsorption experiments, these were performed both in single- and multi-component fashion, using 5 mg of adsorbent (i.e., MIL-100Cr, MIL-101Cr, AC, CMOF-100Cr, or CMOF-101Cr) were mixed water containing the CEC or CECs at a target concentration. The pH of the mixtures was adjusted using sodium hydroxide 0.1 M to obtain a neutral pH (6.5–7.5) and then shaken at 250 rpm for 24 h at room temperature. All these tests were performed in triplicates. Determination of the resulting solution equilibrium concentration and adsorption capacity were also done using the HPLC/MS-MS system described above, along with a CEC mass balance (i.e., Eq. 1). The resulting isotherm data were fitted using the adsorption models of Freundlich and Sips described in the supplementary information.

It is important to note that the adsorbed amounts for all the CEC uptake experiments were normalized by volume of the adsorbent instead of weight because of the difference in bulk density displayed among the adsorbents. For instance, the density of MIL-100Cr is almost four times that of the AC, 1.45 vs. 0.31 g cm^{-3}, respectively. Furthermore, in the case of the CMOFs variants, most if not all the MILs framework phases were effectively grown within the pores of AC due to the confined space synthesis approach, as directly evidenced by their relevant characterization data. This core-shell assembly approach also produces bulk density values that are smaller compared to that of the sole MOF. The density values for the composites were estimated using mass balances on TGA data and using the meso- and macro-porous regions of the PSDs to determine the void volumes of AC that are now occupied by the MOF crystalline phase.

2.6. Adsorbent regeneration tests

The reusability of CMOF-100Cr, the adsorbent material that exhibited superior overall performance, was evaluated using a four (4)-cycle adsorption test. About 20 mg of CMOF-100Cr were mixed with 40 mL of a 500 μg L^{-1} CBZ solution and shaken at room temperature for 24 h. The pH was adjusted to obtain a neutral range at equilibrium conditions, and these tests were also done in triplicates. After the end of the adsorption cycle, the adsorbent was separated using centrifugation and dried in a tubular oven at 50 °C for 3 h under constant nitrogen flow (100 mL min^{-1}). Then, as elucidated from TGA data, a two-stage, sequential thermal treatment was performed under pure nitrogen gas to generate the spent adsorbent. The first stage consisted in bringing the temperature to 100 °C at 10 °C min^{-1} and soaking for 2 h, while the second stage consisting of bringing the temperature to 205 °C and soaking at that point for 12 h. Finally, the recovered solid material was cooled down, characterized by XRD, and then used for another adsorption cycle. The percent of CEC removal was calculated as follows:

$$\%Removal = \frac{C_0 - C_f}{C_0} \times 100 \quad (2)$$

where C_0 and C_f are the initial and final concentrations of CBZ in the aqueous phase, respectively.

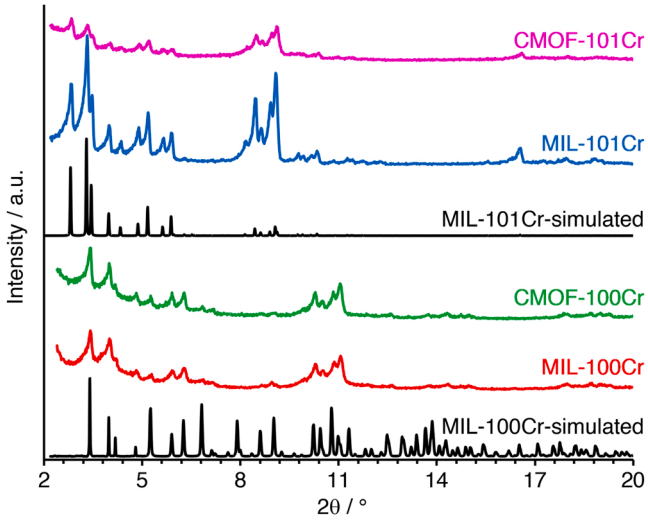

Fig. 1. XRD patterns of MIL-100Cr and MIL-101Cr (simulated and as-synthesized), CMOF-100Cr (as-synthesized), and CMOF-101Cr.

3. Results and discussion

3.1. Materials characterization

A stack of XRD patterns collected for the as-synthesized MOF and CMOF materials is shown in Fig. 1. For reference, the data also include XRD simulated patterns of pure MIL-100Cr and MIL-101Cr. These observations for the as-synthesized MOFs agree with those reported elsewhere [35,42–44]. In the case of the composites, the presence of the desired periodic MOFs phase is corroborated by the perseverance of the XRD principal reflections. However, slight displacements (0.02–0.06°) to higher diffraction angles are observed for the reflections located at 10.22, 10.44, 10.79, and 11.0° for CMOF-100Cr and 2.84, 3.97, 4.88, 5.63, and 10.37° for CMOF-101Cr. These are due to contraction of about 1.5–2.0% in unit cell volume, probably produced by encapsulation of the MOF structure within the AC pores.

SEM-EDAX analyses were used to verify the morphology and bulk elemental composition of the adsorbents materials. Fig. 2 shows micrographs and elemental mappings gathered for CMOF-100Cr, CMOF-101Cr, AC, MIL-100Cr, and MIL-101 Cr. As shown in Figs. 2A and 2B, there is a preponderance of AC (shown as pure in Fig. 2I) in both composites. However, in the case of CMOF-101Cr (Fig. 2F), some octahedral crystals characteristic of the MOF phase can be observed lying onto the AC external surfaces and these are quite smaller than those observed during the synthesis of sole MIL-101Cr (Fig. 2Q). The rest of the MOF phase was grown within the inner meso- and macro-pores of the AC, as evidenced by the content of representative Cr and O in the elemental maps produced by EDAX. The results showed a uniform composition of these two principal constituents of the corresponding MOF unit cell across all the examined areas, but with what appears to be a higher concentration in the case of CMOF-101Cr and probably due to the octahedral MOF crystals seen lying onto the AC external surface. In

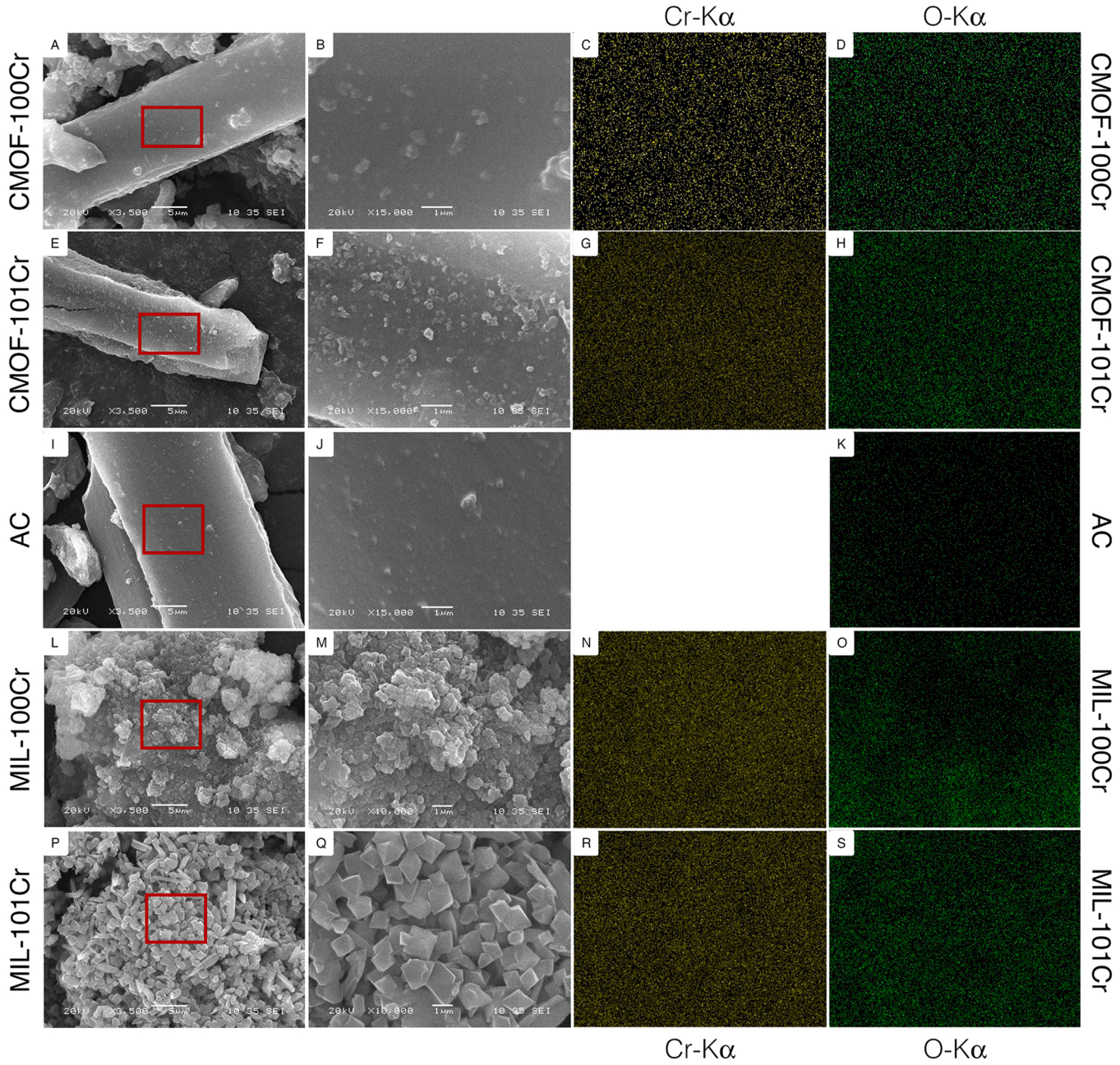

Fig. 2. SEM images of CMOF-100Cr (A), CMOF-101Cr (E), activated carbon AC (I), MIL-100Cr (L), and MIL-101Cr (P), and image magnification corresponding to red colored perimeter areas (B,F,J,M,Q). EDAX mapping for chromium (C,G,N,R) and oxygen (D,H,K,O,S) gathered in the same perimeter areas.

general, these image/compositional data along with XRD provide evidence about the in-situ growth of each MOF inside of the AC. Further evidence of the confined space growth will be presented later in the discussion when assessing the adsorption performance for the composites.

TGA profiles are collected in Fig. 3. Activated carbon shows the elimination of water and guest molecules at ca. 75 °C; another small weight loss is observed between 100 and 350 °C and this could be attributed to the decomposition of functional groups (i.e., -CHO, -OH, and -CO) from the surface [38,39]. Finally, the pyrolysis of the activated carbon starts at a temperature of around ~450 °C. Meanwhile, TGA profiles for the MOF materials (i.e., MIL-100Cr and MIL-101Cr) present a significant weight loss (ca. 40 – 50 wt%) that corresponds to the elimination of free water, and perhaps other guest molecules, at around 100 °C. An additional weight loss (4 – 5 wt%) produced by eliminating water molecules that are coordinated to the metal node can be seen between 100 and 300 °C. The decomposition of the organic linkers (i.e., trimesic and terephthalic acid ~36 wt%) and, therefore, the collapse of the structural scaffold [35], starts at a temperature of about 300 °C. This breakdown and subsequent evacuation developed stepwise, which is typical for organic molecules/transition metal arrangements. The residues observed at the end of the TGA profiles correspond to chromium oxides. In general, the observed weight losses commensurate very well with those that correspond to the chemical formulae of MIL-100Cr ($Cr_3F(H_2O)_2O((C_6H_3)\text{-}(CO_2)_3)_3$. nH_2O, n = ~16) and MIL-101Cr ($Cr_3F(H_2O)_2O((C_6H_4)\text{-}(CO_2)_2)_3$. nH_2O, n = ~30) [35,43].

In the case of the composites (i.e., CMOF-100Cr and CMOF-101Cr), the stepwise weight losses observed in the TGA profiles are similar to the corresponding pure MOF phases. However, the weight losses of free and coordinated water (~7 wt% for CMOF-100Cr and 18 wt% for CMOF-101Cr) are less, which could be related to the hydrophobic nature of AC. In fact, contact angle tests (see Fig. 4) showed that the AC transferred its' hydrophobic character to the composite CMOF-100Cr. According to the TGA profiles, the decomposition of the organic linkers was displaced from 300° to 400°C, and this is related to the additional energy needed to decompose and evacuate molecules confined inside the activated carbon pores [49]. A mass balance using an anhydrous basis was also used to determine the composition of the composites' constituent materials (i.e., MOF and AC). This balance was developed considering that the weight step loss of the organic linker is given exclusively by the MOF phase. As a result, CMOF-100Cr is composed of ca. 56 wt% of MIL-100Cr, while in CMOF-101Cr, ca. 63 wt % is MIL-101Cr. These data, however, do not suffice to estimate the occupancy of AC voids by the corresponding MOF and that will be presented later in the discussion as part of the PSD results.

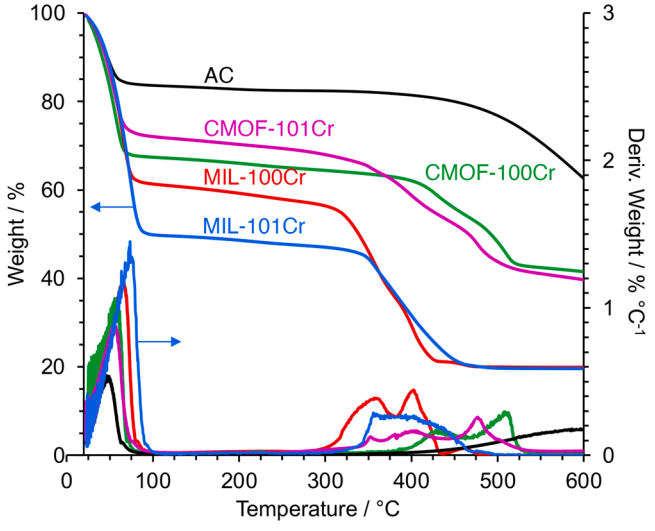

Fig. 3. . Thermal gravimetric analysis weight loss and derivative weight loss profiles for AC, MIL-100Cr, and CMOF-100Cr. Data gathered under pure nitrogen.

In general, similar TGA behaviors have been observed for isoreticular MIL-100Fe (see Fig. S1) [38]. However, it should be noted that MIL-100Cr has lower thermal stability probably because of the coordination forces between the organic linker (trimesic acid) and the metal nodes (i.e., Cr vs. Fe). The coordination strength and possible implications will be further discussed later in the XPS analysis section below.

Nitrogen adsorption–desorption equilibrium isotherms were gathered at −196 °C for all the adsorbent materials, and the data are shown in Fig. S2. The uptake amounts were also normalized by volume of adsorbent instead of weight to provide accurate textural properties comparisons (i.e., surface area and pore volume). It should be noted that both composites exhibited a hybrid type I/IV isotherm behavior (isotherm classifications based on IUPAC), indicating that the high microporosity from MOFs structures remains in the composites while the hysteresis gap seen in apohost AC is nearly absent. The disappearance of this gap is evidence of the occupancy of the meso- and macropores of the AC by the MOF phases. Pore size distribution (PSD) profiles were also estimated from the aforementioned nitrogen adsorption-desorption data, and the results are shown in Fig. 5.

The microporous region (< 20 Å) of the PSD was estimated using the HK-CY approach, while the meso- (20 – 200 Å) and macro-porous (> 200 Å) regions were estimated via the BJH method. The resulting micropores for AC are ~5.0 and 7.5 Å in size and the material also contains a wide range of meso and macro-pores sizes. For MIL-100Cr, the estimated pore sizes are 5, 8, 21, and 25 Å, while for MIL-101Cr, these are 11, 31, and 35 Å. These values match those reported elsewhere [50]. In the case of the composites, the microporous regions corresponding to the MOF phases are still present, but most or all of the meso- and macropores from AC are not. This is due to the occupancy of the MOF within the AC in the composite. Interestingly, the micropores of AC are also absent in CMOF-101Cr, but the AC pores of diameter about ~46 Å remained in both CMOFs materials. This is probably due to the lengths of the MOF crystal seeds during the early aging stages of the confined synthesis. Characteristic lengths of the unit cells of the MOFs (72.9 Å in MIL-100Cr and 88.8 Å in MIL-101Cr) [35,43] suggest that the AC's pores of 46 Å width are probably sterically restrictive for proper growth and subsequent occupancy by the MOF phases.

The nitrogen adsorption-desorption isotherms and PSD data were also used to estimate BET surface area values, along with total pore volume, occupancy of meso- and macro-pores by the MOFs, and density (Table 1). Occupancy of the AC meso- and macro-pores by the corresponding MOF was estimated relating the areas under the PSD profiles of each material, which were obtained via integration of the corresponding regions (AC vs. CMOFs), and under the consideration that the area reduction was exclusively due to the presence of the MOFs. In the case of CMOF-100Cr, 100% of the AC meso- and macro-pores are occupied by MIL-100Cr. However, only 43% of the meso- and macro-pores of AC were filled with MIL-101Cr (see Table 1); this is evidence that a portion of this MOF's crystals grew outside the AC voids; this matches qualitatively very well with the SEM image shown in Fig. 2F. At this point, it is important to mention that usage of larger AC contents during synthesis brings restriction to the crystallization process of the MIL-101Cr and would yield only an amorphous phase.

Fig. 6 shows high-resolution XPS spectra of Cr2p for the MOFs and CMOFs. The Cr2p spectra for single-phase MOFs can be deconvoluted into two (2) principals peaks, each centered at 577.5 and 586.7 eV (ΔBE = 9.2 eV) and corresponding to $2p_{3/2}$ and $2p_{1/2}$ orbitals, respectively. These also corroborate the expected presence of Cr^{+3} in the structure [51–53]. Interestingly, the displacement between the binding energy of the $Cr2p_{3/2}$ in MIL-100Cr and the standard value is only 3.1 eV [54], unlike the 18.7 eV displacement observed for isoreticular MIL-100Fe for $Fe2p_{3/2}$ [38]. This is probably related to the relatively smaller thermal stability of MIL-100Cr compared to MIL-100Fe (see Fig. S1); since the Cr

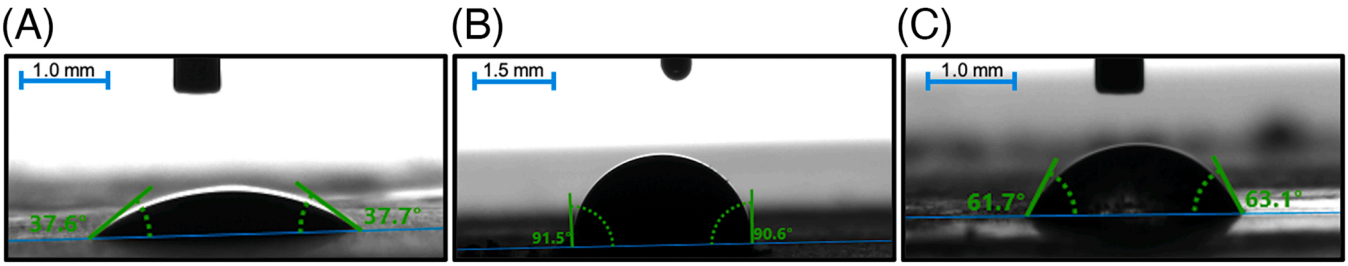

Fig. 4. Water contact angle measurements for (A) MIL-100Cr, (B) AC, and (C) CMOF-100Cr.

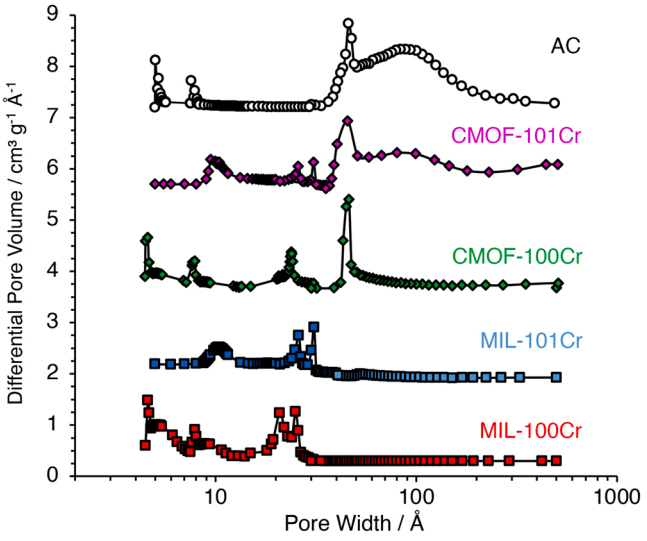

Fig. 5. Pore size distribution profiles estimated from the nitrogen adsorption–desorption isotherms gathered at 196 °C for MIL-100Cr, MIL-101Cr, CMOF-100Cr, CMOF-100Cr, and activated carbon. Microporous region estimated using corrected Horvath-Kawasoe method and meso- and macroporous region using the BJH desorption method.

Table 1
Selected textural and compositional properties of AC, MOFs, and CMOFs.

Material	Density (g cm^{-3})	BET Surface Area[a]		Pore Volume[a] (cm^3 cm^{-3})	Occupancy of Meso- & Macro-pores by MOF[b] (%)
		(m^2 g^{-1})	(m^2 cm^{-3})		
AC	0.31	1296	402	0.39	0
MIL-100Cr	1.45[35]	1673	2426	1.36	–
CMOF-100Cr	0.70[c]	1550	1085	0.58	100
MIL-101Cr	0.62[43]	2249	1394	0.82	–
CMOF-101Cr	0.57[c]	1135	643	0.55	43

[a] Estimated from N_2 adsorption–desorption isotherms data gathered at −196 °C.
[b] Values Estimated from TGA and PSD data.
[c] Values estimated from TGA and N_2 adsorption–desorption isotherms.

node is plausibly less coordinated to the organic linkers, this could also imply a more robust projection of an electrostatic energy field within the effective pore surface of MIL-100Cr and toward guest molecules such as adsorbates.

For CMOF-100Cr and CMOF-101Cr, deconvolution for Cr2p resulted in two peaks centered at 577.7 and 587.1 eV corresponding to $2p_{3/2}$ and $2p_{1/2}$, respectively. This is also a slight variation in binding energy for CMOFs compared to sole MOFs and could be associated with weak interactions taking place between the MOFs phase and the AC surface.

These characterization results provided further direct evidence of the occupancy of the MOFs phase in the void pores of activated carbon.

Zeta potential profile measurements are shown in Fig. 7. The profile obtained for AC showed a negative behavior at pH greater than 4.0, while at lesser pH values, a weak positive character was observed. These agree with data reported for carbon materials activated similarly to Darco KB-G [37,55,56]. On the other hand, the zeta potential profile for MIL-100Cr exhibited a strong negative character at a wide range of pH, including the neutral region (IEP ~3.5), while the MIL-101Cr net surface charge showed to be strongly positive up to a pH of ca. 8.2. These results also agree with values published elsewhere [42,57]. In the case of the CMOF-100Cr composite, the strong negative behavior from the MIL-100Cr phase apparently dominated the overall surface charge profile of the composite. For CMOF-101Cr, Fig. 7 shows an intermediate behavior at pH < 6, one that lies between MIL-101Cr and AC; at higher pH, a slightly more negative character was observed.

4. Single component CEC adsorption tests

Transient fractional uptake profiles for adsorption of CBZ onto MIL-100Cr and CMOF-100Cr are shown in Fig. S3. The data showed no significant phenomenological impediment during the adsorption of CBZ since the equilibrium conditions were reached within minutes in both adsorbents. Also, the corresponding estimated diffusion coefficients were 5.12×10^{-17} and 2.81×10^{-16} m^2 s^{-1} for MIL-100Cr and CMOF-100Cr, respectively.

Fig. 8 shows single point equilibrium loadings for CBZ (C_e ~10 μg L^{-1}) in different adsorbents, including one produced from a direct physical mixture of MIL-100Cr and AC at weight proportions similar to those seen in CMOF-100Cr (see Table 1). The data clearly show the advantage of using a confined synthesis approach to prepare the composite (i.e., CMOF-100Cr; 10.58 mg CBZ cm^{-3} at C_e ~10 μg L^{-1}), with two orders of magnitude gain compared to the CBZ uptake in sole MIL-100Cr and a three-fold (3x) increase compared to AC. Compared to the CMOF-100Fe composite reported previously by our group (1.47 mg CBZ cm^{-3} at C_e ~10 μg L^{-1}) [38], the enhancement in loading provided by CMOF-100Cr at the same concentration is more than seven-fold (7x). In the case of the physical mixture of MIL-100Cr and AC, the smaller gain obtained over sole MIL-100Cr is due to the presence of AC, but there is no synergistic increase in CBZ loading (i.e., no MOF surface protected from water). It should be noted that the loadings reported in this study never exceeded those allowed by the voids of the adsorbents materials, including the composite. For example, a CBZ loading of 10 mg cm^{-3} (or 10,000 μg cm^{-3}) onto CMOF-100Cr is equivalent to an adsorbed CBZ volume of 0.01 cm^3 cm^{-3}, which is well below the saturation of the pore volume available in CMOF-100Cr (see Table 1).

Fig. 9 (left column) shows single-component equilibrium adsorption isotherms gathered at ambient conditions and neutral pH. The data were fitted using Freundlich and Sips isotherm models, and the fits and estimated parameters are shown in Fig. S4 and Table S2, respectively. MIL-

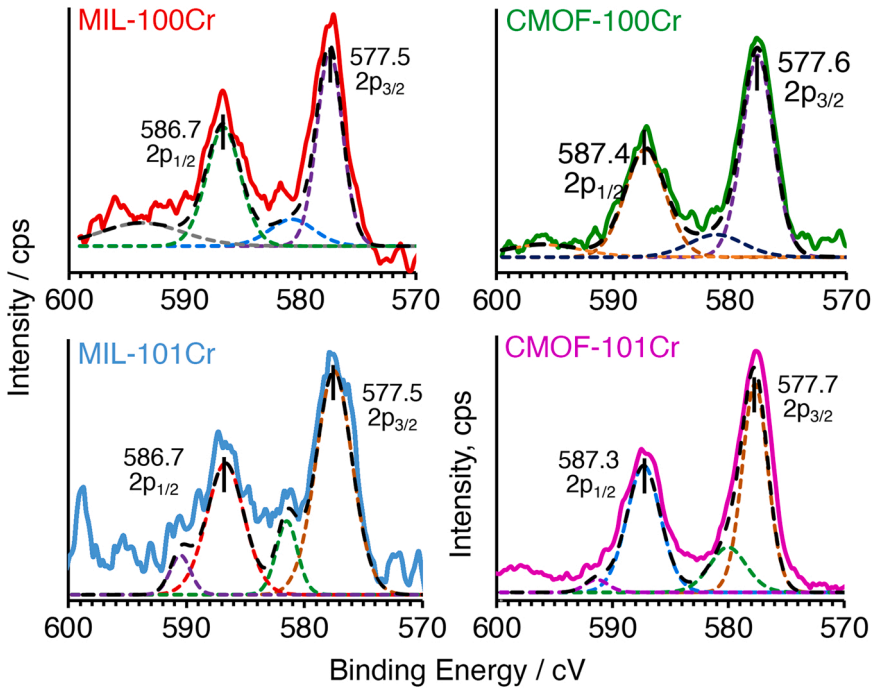

Fig. 6. High resolution XPS spectra of Cr2p for MIL-100Cr, CMOF-100Cr, MIL-101Cr and CMOF-101Cr.

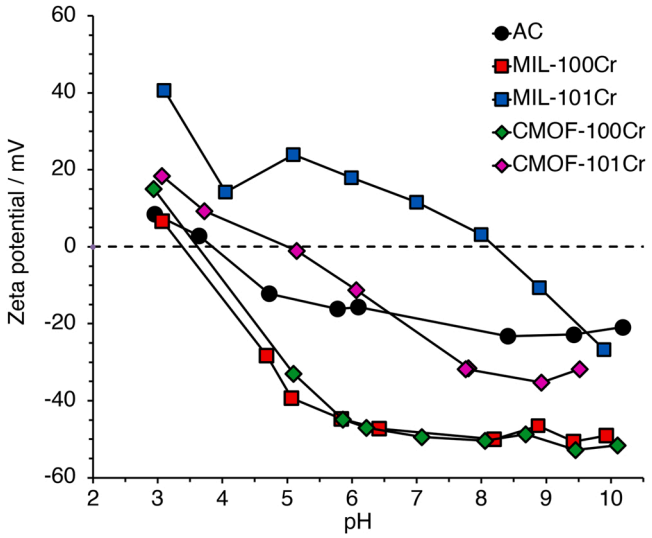

Fig. 7. Zeta potential profiles with respect to pH for AC, MIL-100Cr, MIL-101Cr, CMOF-100Cr, and CMOF-100Cr.

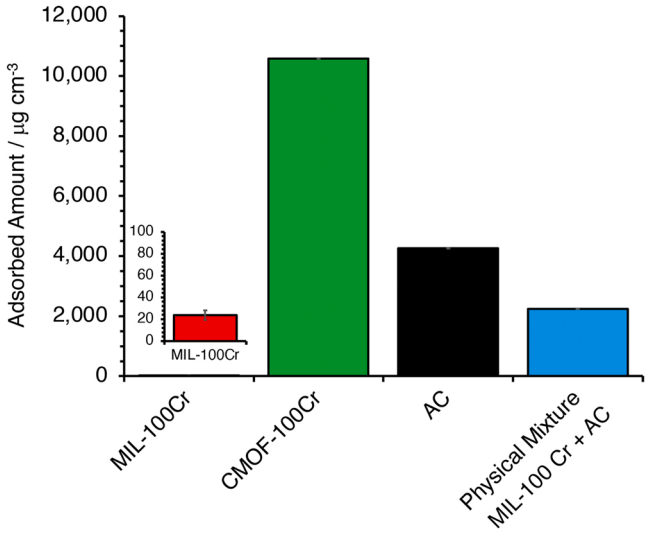

Fig. 8. Single point loadings for adsorption of carbamazepine (C_e ~10 µgL^{-1}) onto MIL-100Cr, CMOF-100Cr, activated carbon, and physical mixture of MIL-100Cr and AC at ambient temperature.

100Cr adsorbent showed a good capacity for contaminants with no ionic charge in solution (i.e., CFN, PXN, CBZ, and Ep-CBZ). This could be attributed mainly to the presence of electrostatic, hydrogen bonding, π–π stacking, and homosynthon interactions (interactions between a pair of identical functional groups) [58–60] between the adsorbent surface and the CEC. Interestingly, CA and NPX showed adsorbed amounts comparable to CBZ, which could be due to the distribution of electronic charges on the CEC molecule structure. Qin, et. al. [61] reported that electron donor (i.e., isopropoxy group) and electron withdrawer (i.e., chlorine substituent) regions are diametrically located in CA molecule, thus, the negative charge of the MIL-100Cr surface could be interacting with the isopropoxy group. The poor affinity of the MOF toward *o*-DMN, contrary to what is seen for NPX, could be explained by the difference in Gibbs's free energy (−767.36 and −728.08 Ha for NPX and *o*-DMN), where more negative values promote spontaneous binding and interactions. Another relevant factor that might explain this behavior is the HOMO-LUMO energy gap, where large values are responsible for high kinetic stability and low chemical activity; the corresponding values are + 3.04 eV for NPX and + 4.47 eV for *o*-DMN [62]. Meanwhile, the lack of interaction between MIL-100Cr and SA could also be explained by the repulsion of electrostatic charges between the net negative surface charge and the deprotonated acid, as well as the HOMO-LUMO energy gap (+5.38 eV) [63].

In the case of MIL-101Cr, the positive net surface charge (Fig. 7) promotes interactions with the deprotonated adsorbates such as NPX and *o*-DMN. In contrast, the other two deprotonated CECs, SA and CA, showed smaller adsorption loadings in MIL-101Cr, suggesting that the electrostatic forces do not constitute the primary or underlying

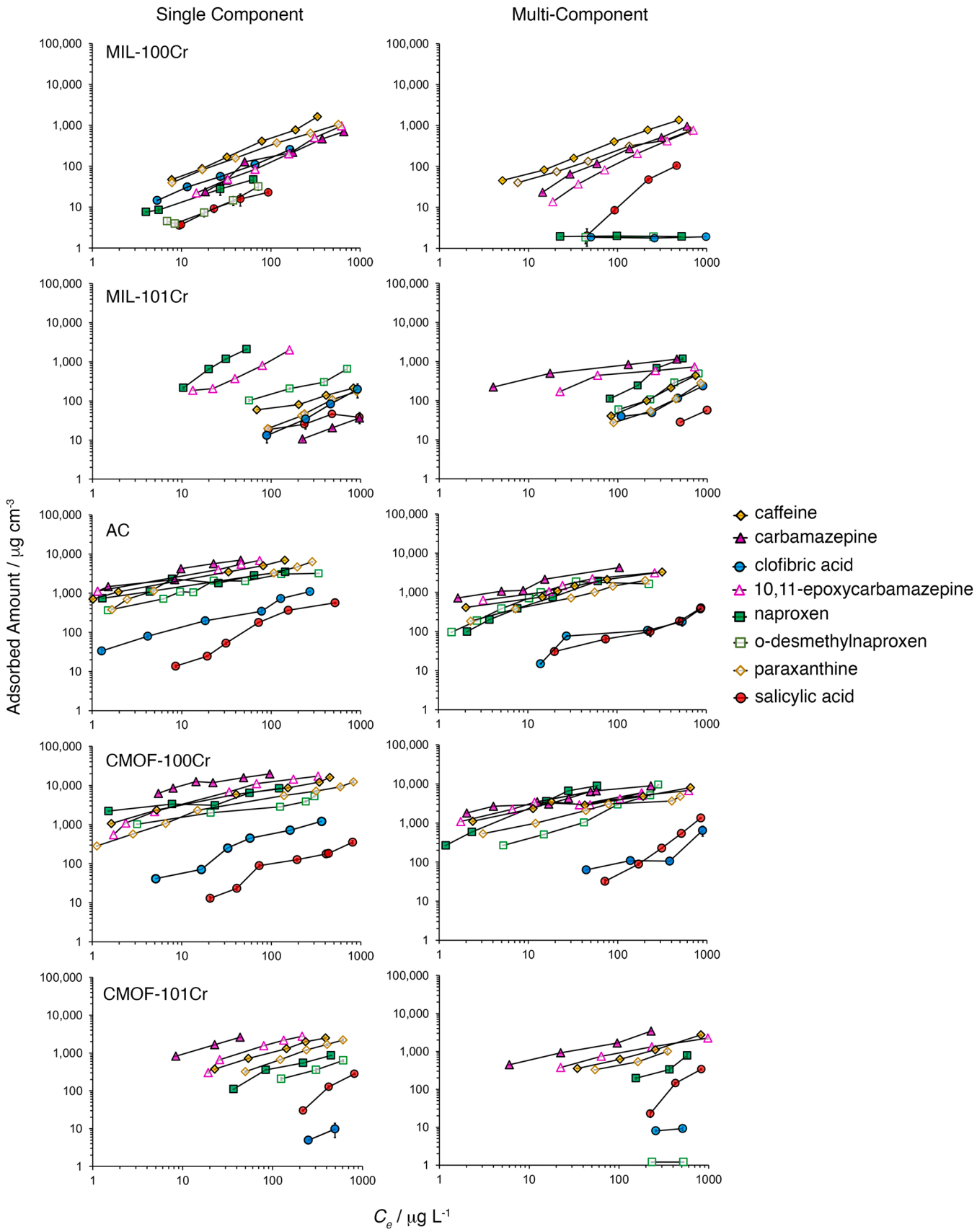

Fig. 9. Single-component (left) and multi-component (right) equilibrium adsorption isotherms onto MIL-100Cr, MIL-101Cr, activated carbon, CMOF-100Cr, and CMOF-101Cr. Data were gathered at ambient temperature and neutral pH.

adsorption mechanism, but rather hydrogen bonding or homosynthon interactions. This is further evidenced by the superior adsorption capacity of MIL-101Cr for Ep-CBZ compared to CBZ, carbamazepine, and due to the epoxide group located in the former that results in better hydrogen donor-receptor capacity [64]. Adsorption capacities observed for CFN and PXN were similar.

AC showed a good capacity for the adsorption of CFN, CBZ, NPX, and metabolites Ep-CBZ, *o*-DMN, and PXN. The plausible mechanism that can explain the affinity of AC is the hydrophobic interaction [65], even for contaminants with a low K_{ow} coefficient (such as CFN and PXN). In addition, the functional groups available on the surface of activated carbons (i.e., hydroxyl, carboxyl, carbonyl) [66] can also offer electron donor-acceptor and homosynthon interactions [17,67–69]. Further evidence that suggests that hydrophobic interactions dominate in AC is the comparable adsorption capacity observed for NPX and its metabolite (e.g., 1.81 and 2.09 mg cm^{-3} for *o*-DMN at ~20 μgL^{-1}). In this case, the less electron donor character produced by the loss of the methyl group did not affect the adsorption. Meanwhile, the adsorption of CFN and PXN is probably governed by electrostatic interaction between the cationic caffeine species and the polarized moieties from the adsorbent surface [59,70,71]. On the other hand, CA and SA resulted in lower adsorption capacities on AC, probably because both acids experienced electrostatic repulsion. Despite this, the AC capacity toward the acids is greater than both MOFs, corroborating the great importance of the hydrophobic character of an adsorbent.

In the case of CMOF-100Cr, and as discussed at the beginning of this section (i.e., Fig. 8), an outstanding adsorption capacity for CBZ was observed. This can be explained not only from the material hydrophobicity point of view, but also based on specific interactions such as hydrogen bonding or π−π stacking offered by the MIL-100Cr phase that resides within the pores of AC. For NPX and *o*-DMN, the composite adsorbed about 4.1 and 2.0 mg cm^{-3}, respectively, at an equilibrium concentration of 20 μg L^{-1} and such difference is probably due to the higher electron donor character produced by the end methyl group of NPX. On the other hand, the observed enhancement in the adsorption of CFN and PXN compared to AC can be due to the stronger negative surface charge and the high density of homosynthon functional groups both present in CMOF-100Cr (see Figs. 6 and 7). Finally, the adsorption of CA appears to be supported by the individual contributions of hydrophobic interaction from the AC shell and electron donor-acceptor mechanism from the MIL-100Cr core in the composite. SA was the least adsorbed CEC in CMOF-100Cr, and this can be related to the high kinetic stability yet poor chemical activity of the adsorbate.

The results obtained for CMOF-101Cr, in general, showed single-component adsorption capacity that increases as follows: CA< SA < *o*-DMN < NPX < PXN < CFN < Ep-CBZ < CBZ. Unlike the case of sole MIL-101Cr, where the CBZ loadings were the smallest ones observed, the CBZ adsorption capacity in CMOF-101Cr was the largest, probably because of the contribution of the hydrophobic interactions from AC. Interestingly, the CBZ adsorption capacity is well below the levels achieved by the CMOF-100Cr counterpart, and this could be very much due to the lesser occupancy of the AC large voids by MIL-101Cr (see Table 1). At 20 μg L^{-1}, the CBZ adsorption capacity in CMOF-101Cr is about 1.65 mg cm^{-3} with just 43% occupancy of the MOF, and consequently, there is room for improvement. However, the growth of the MIL-101Cr appears to be severely limited by faster aging rates during crystal growth. It will therefore require more efforts to elucidate the paths to achieve 100% occupancy of the AC large voids by MIL-101Cr.

It is worth to mention again that by improving the hydrophobic character of a composite via confined space synthesis, the amount of water molecules that interact with the MOF is considerably decreased and this significantly increases the interactions of CECs with the MOF active adsorption sites. MOFs containing a high density of active adsorption sites, such as MIL-100Cr [44,72], should promote superior adsorption capacity in hierarchical environments that provide a hydrophobic shell.

Table S3 collects CEC adsorption capacities of various porous adsorbents for the same set of CECs reported at an equilibrium concentration of near 20 μg L^{-1} or the nearest closed value. These were extracted from literature that worked at a similar concentration range of adsorbate or extrapolated using reported isotherm parameters. The materials range includes carbons, clay, silica, zeolites, and MOFs. As can be seen from the data, CMOF-100Cr showed the largest uptake capacities for the CECs considered here, with the only exception being SA.

4.1. Multiple component CEC adsorption tests

Fig. 9 (right column) also gathers equilibrium adsorption isotherm data from multi-component CEC batch uptake experiments. As expected, competition between CECs that are present simultaneously in water samples produced a decrease in the overall adsorption capacities compared to the results seen in single-component adsorption tests. To aid in the visualization of this, Fig. 10 shows accumulative adsorption capacities for the adsorbents at an equilibrium concentration of the corresponding CEC of 20 μg L^{-1}. CMOF-100Cr maintained similar adsorption capacities for NPX and CFN in both scenarios (i.e., single- and multi-component), but a reduction of about 70% in capacity was observed for o-DMN or SA. By contrast, the adsorption capacities in AC decreased by 58% and 53% for NPX and CFN, respectively, but increased by 19% and 24% for o-DMN and SA.

4.2. Distinct mechanism for carbamazepine adsorption onto CMOF-100Cr

An attempt to elucidate the possible interaction mechanisms that are taking place during the adsorption of CBZ onto AC (CBZ@AC) and CMOF-100Cr (CBZ@CMOF-100Cr) was made via *ex situ* XPS analysis. For this, it was assumed that the characteristic atoms interacting during the adsorption of CBZ were O and N in the case of CBZ@AC and Cr and N in CBZ@CMOF-100Cr. The XPS spectra gathered for these tests are shown in Fig. 11. XPS spectra for fresh, non-adsorbed CBZ is shown in Fig. S5 for reference.

The Cr2p spectrum showed a displacement from 577.6 to 576.8 eV for the $2p_{3/2}$ peak and from 587.4 to 586.6 eV for the $2p_{1/2}$ peak (see Fig. 6 and Fig. 11). These slight displacements can be associated to interactions between the adsorbents and the CBZ terminal -NH_2 group [54]. Similar binding energies reductions have been observed for the interaction of CBZ with transition metals contained in MOFs [73]. A deconvolution of the N1s spectrum from the CBZ adsorbed onto CMOF-100Cr shows peaks centered at 396.1, 397.8, 399.4, and 401.1 eV. The first two can be related to interactions with Cr in MIL-100 [54], while the third peak corresponds probably to the azepine nitrogen [74] and the fourth corresponds to the nitrogen interacting with carboxylic groups from the AC surface and the organic linker in MIL-100Cr, both in the CMOF-100Cr composite [74].

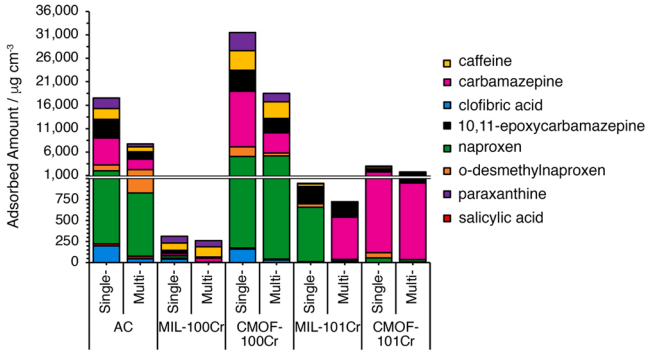

Fig. 10. Adsorption capacity at an equilibrium concentration of adsorbate of 20 μg $L^{-1}$for AC, MIL-100Cr, CMOF-100Cr, MIL-101Cr, and CMOF-101Cr.

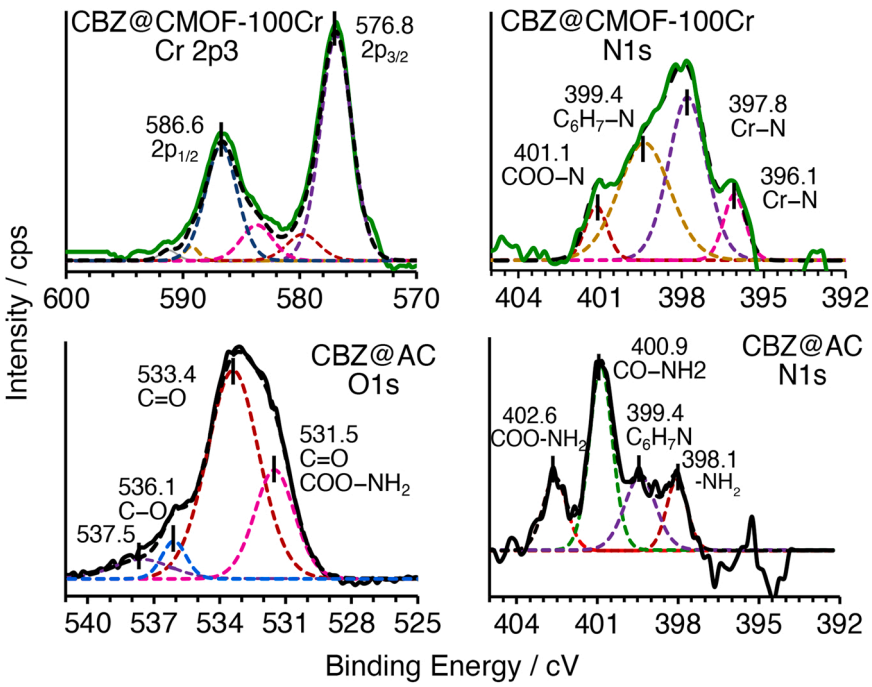

Fig. 11. High-resolution XPS spectra for the pairs CBZ@CMOF-100Cr and CBZ@AC. CMZ adsorbed onto the AC or CMOF-100Cr at ambient temperature.

In the case of the CBZ adsorbed onto AC, besides of hydrophobic interaction [75], the spectrum for O1s shows an intensification of the peak centered at 531.5 eV, which is associated with C═O groups and COO-NH_2 interactions [74]. The N1s spectrum shows the appearance of peaks centered at 400.9 and 402.6 eV, which can be attributed to CO-NH_2 and COO-NH_2 interactions [54], while the peaks corresponding to the azepine nitrogen (~399.4 eV) remained.

The differences in the binding energies observed for the N1s spectra of the adsorbed CBZ confirms dissimilar adsorption mechanism in CMOF-100Cr and AC. The adsorption in CMOF-100Cr is not just governed by the hydrophobic interactions given by AC, but also by the possible π–π interactions offered by the active metal site (i.e., Cr^{3+}). Scheme 2 includes depictions of what are the apparent adsorption mechanisms taking place in the aforementioned cases.

4.3. CMOF-100Cr regeneration

Since the largest adsorption capacity observed for CBZ in this study took place in CMOF-100Cr, the feasibility of thermal regeneration under nitrogen gas at 205°C was evaluated as an alternative to ensure the recyclability of this material. Please refer to the Experimental Section above for details. It is worth to notice that the melting point of most of the organic pollutants tested here lies between 150 and 200 °C (see Table S1). In addition, MIL-100Cr is characterized by having great stability at temperatures as high as 300 °C (see Fig. 3), which can furnish the CMOF-100Cr with the potential for thermal regeneration. Fig. 12 shows removal capacities for adsorption of CBZ onto fresh and thermally regenerated CMOF-100Cr, along with the corresponding adsorbent XRD pattern. The results show that complete removal of CBZ from water is possible after thermal regeneration of spent CMOF-100Cr up to at least fourth cycles, while XRD patterns display no changes in the structural conformation of the confined composite phase (i.e., MIL-100Cr) after the third cycle of regeneration. These results confirm the viability of a thermal regeneration strategy as applied to CMOF-100Cr.

5. Conclusions

Chromium-based MOFs (MIL-100Cr and MIL-101Cr) were each grown within the voids of an activated carbon (AC) and evaluated in the adsorption of CECs from water. A comprehensive characterization of the resulting hierarchical composites (CMOF-100Cr and CMOF-101Cr) corroborated the occupancy of the meso- and macro-pores of the carbon by the corresponding MOF (100% and 43% for CMOF-100Cr and CMOF −101Cr, respectively). CEC adsorption data also demonstrated

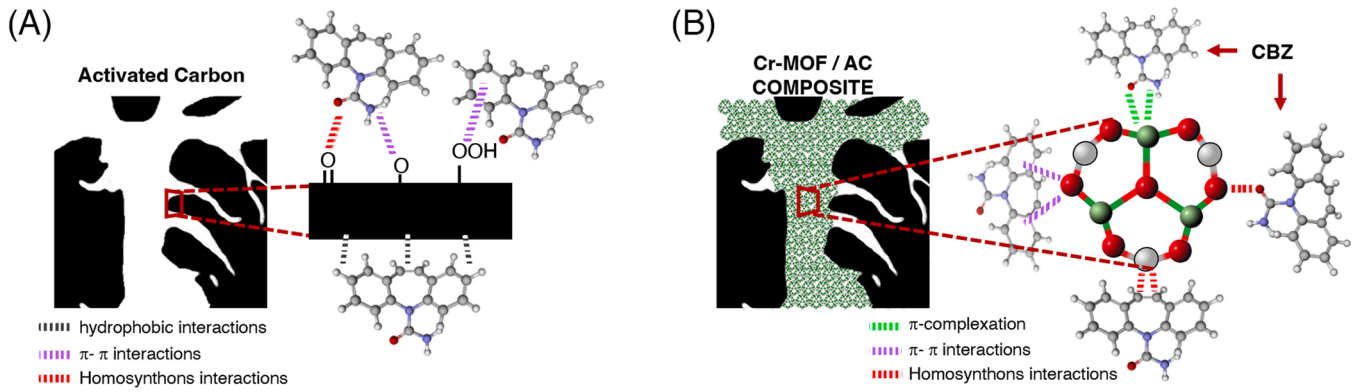

Scheme 2. Apparent CBZ uptake mechanism onto (A) AC or (B) CMOF according to XPS observations.

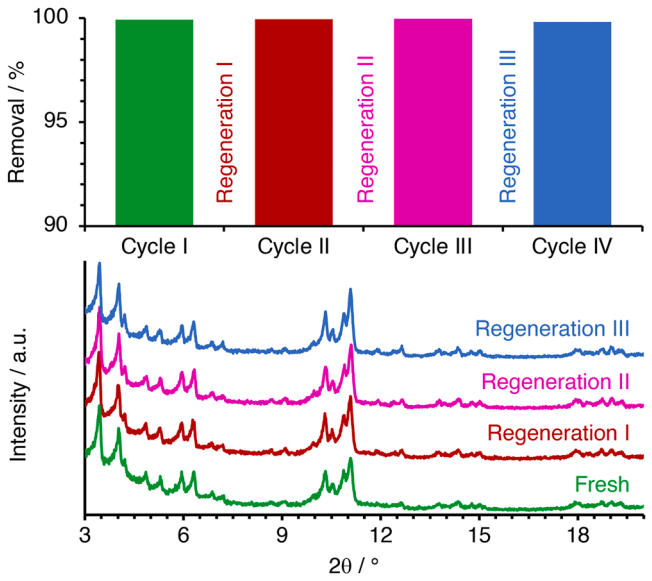

Fig. 12. Removal of CBZ using CMOF-100Cr as adsorbent (top) and XRD patterns of CMOF-100Cr (bottom) after thermal regeneration. Thermal treatment performed under nitrogen under a ramp and soak program up to 205 °C.

that the organic linkers present in the MOFs (i.e., benzene-1,3,5-tricarbox1yc acid or benzene-1,4-dicarboxylic acid) does influence the uptake capacities. For example, single-component CEC adsorption revealed that the highest capacity of MIL-100Cr was for CFN, while for MIL-101Cr it was for NPX. Meanwhile, CMOF-100Cr showed an outstanding adsorption capacity for CBZ, almost triple that of AC and orders of magnitude larger compared to the other adsorbents prepared and tested in this study. This was mainly due to the hydrophobic shell created by the AC in the composite to allow the surface of the core MIL-100Cr to interact with the CEC without much competition from water uptake. Compared to the CMOF-100Fe composite previously reported by our group, the enhancement in CBZ loading provided by substituting the Fe metal node for Cr is more than seven-fold at C_e ~10 μg L^{-1}. As supported by XPS data, the improvement in capacity was due to interactions between the chromium node in the MIL-100Cr phase of the CMOF-100Cr composite and the nitrogen atoms of CBZ. This differs from what is observed in sole AC, where the interactions are primarily between the surface and the oxygen from the functional groups. Finally, a thermal treatment under nitrogen at 205°C was successful in regenerating the CMOF-100Cr, which showed no loss in CBZ uptake capacity after at least for cycles.

CRediT authorship contribution statement

Juan C. Muñoz-Senmache: Conceptualization, Methodology, Investigation, Formal analysis, Writing – original draft. **Perla E. Cruz-Tato:** Methodology, Investigation. **Eduardo Nicolau:** Methodology, Investigation. **Arturo J. Hernández-Maldonado:** Conceptualization, Methodology, Investigation, Writing – review & editing, Visualization, Project administration, Funding acquisition.

Declaration of Competing Interest

The authors declare that they have no known competing financial interests or personal relationships that could have appeared to influence the work reported in this paper.

Acknowledgments

Support for this project was provided by the National Science Foundation (NSF) under Grant No. OIA-1632824 and by the National Aeronautics and Space Administration (NASA) under Grant No. 80NSSC19M0236. The authors acknowledge the UPR Materials Characterization Center (MCC) for the provided support during the SEM analysis. Finally, the authors wish to express gratitude to undergraduate students Ms. Anaira Roman-Santiago and Mr. Isaac Ramirez-Marrero for their help in the laboratory activities during the synthesis of MIL-100Cr and CMOF-100Cr.

Appendix A. Supporting information

Supplementary data associated with this article can be found in the online version at doi:10.1016/j.jece.2022.107282.

References

[1] R. Akhbarizadeh, S. Dobaradaran, T.C. Schmidt, I. Nabipour, J. Spitz, Worldwide bottled water occurrence of emerging contaminants: a review of the recent scientific literature, J. Hazard. Mater. 392 (2020), 122271, https://doi.org/10.1016/j.jhazmat.2020.122271.
[2] S. Gonzalez-Rubio, A. Ballesteros-Gomez, A.G. Asimakopoulos, V.L.B. Jaspers, A review on contaminants of emerging concern in European raptors (2002-2020), Sci. Total Environ. 760 (2021), 143337, https://doi.org/10.1016/j.scitotenv.2020.143337.
[3] T.K. Kasonga, M.A.A. Coetzee, I. Kamika, V.M. Ngole-Jeme, M.N.B. Momba, Endocrine-disruptive chemicals as contaminants of emerging concern in wastewater and surface water: a review, J. Environ. Manag. 277 (2021), 111485, https://doi.org/10.1016/j.jenvman.2020.111485.
[4] S. Ofori, A. Puskacova, I. Ruzickova, J. Wanner, Treated wastewater reuse for irrigation: pros and cons, Sci. Total Environ. 760 (2021), 144026, https://doi.org/10.1016/j.scitotenv.2020.144026.
[5] Y.K. Tang, Y.X. Zhong, H.L. Li, Y.T. Huang, X.Y. Guo, F. Yang, Y. Wu, Contaminants of emerging concern in aquatic environment: occurrence, monitoring, fate, and risk assessment, Water Environ. Res 92 (2020) 1811–1817, https://doi.org/10.1002/wer.1438.
[6] W.T. Vieira, M.B. de Farias, M.P. Spaolonzi, M.G.C. da Silva, M.G.A. Vieira, Endocrine-disrupting compounds: Occurrence, detection methods, effects and promising treatment pathways: a critical review, J. Environ. Chem. Eng. 9 (2021), 104558, https://doi.org/10.1016/j.jece.2020.104558.
[7] J. Maculewicz, D. Kowalska, K. Swiacka, M. Tonski, P. Stepnowski, A. Bialk-Bielniska, J. Dolzonek, Transformation products of pharmaceuticals in the environment: their fate, (eco)toxicity and bioaccumulation potential, Sci. Total Environ. 802 (2022), 149916, https://doi.org/10.1016/j.scitotenv.2021.149916.
[8] S. Zhang, S. Gitungo, L. Axe, J.E. Dyksen, R.F. Raczko, A pilot plant study using conventional and advanced water treatment processes: Evaluating removal efficiency of indicator compounds representative of pharmaceuticals and personal care products, Water Res. 105 (2016) 85–96, https://doi.org/10.1016/j.watres.2016.08.033.
[9] T. Rasheed, M. Bilal, A.A. Hassan, F. Nabeel, R.N. Bharagava, L.F. Romanholo Ferreira, H.N. Tran, H.M.N. Iqbal, Environmental threatening concern and efficient removal of pharmaceutically active compounds using metal-organic frameworks as adsorbents, Environ. Res. 185 (2020), 109436, https://doi.org/10.1016/j.envres.2020.109436.
[10] D.M. Revitt, L. Lundy, D. Fatta-Kassinos, Development of a qualitative approach to assessing risks associated with the use of treated wastewater in agricultural irrigation, J. Hazard. Mater. 406 (2021), 124286, https://doi.org/10.1016/j.jhazmat.2020.124286.
[11] P.R. Rout, T.C. Zhang, P. Bhunia, R.Y. Surampalli, Treatment technologies for emerging contaminants in wastewater treatment plants: a review, Sci. Total Environ. 753 (2021), 141990, https://doi.org/10.1016/j.scitotenv.2020.141990.
[12] F. Mansour, M. Al-Hindi, R. Yahfoufi, G. Ayoub, M. Ahmad, The use of activated carbon for the removal of pharmaceuticals from aqueous solutions: a review, Rev. Environ. Sci. Biotechnol. 17 (2018) 109–145, https://doi.org/10.1007/s11157-017-9456-8.
[13] M. Patel, R. Kumar, K. Kishor, T. Mlsna, C.U. Pittman, D. Mohan, Pharmaceuticals of emerging concern in aquatic systems: Chemistry, occurrence, effects, and removal methods, Chem. Rev. 119 (2019) 3510–3673, https://doi.org/10.1021/acs.chemrev.8b00299.
[14] D. Akhil, D. Lakshmi, P.S. Kumar, D.V.N. Vo, A. Kartik, Occurrence and removal of antibiotics from industrial wastewater, Environ. Chem. Lett. 19 (2021) 1477–1507, https://doi.org/10.1007/s10311-020-01152-0.
[15] L.J. Huang, R.J. Shen, Q. Shuai, Adsorptive removal of pharmaceuticals from water using metal-organic frameworks: a review, J. Environ. Manag. 277 (2021), 111389, https://doi.org/10.1016/j.jenvman.2020.111389.
[16] M.K. Shahid, A. Kashif, A. Fuwad, Y. Choi, Current advances in treatment technologies for removal of emerging contaminants from water: a critical review, Coord. Chem. Rev. 442 (2021), 213993, https://doi.org/10.1016/j.ccr.2021.213993.
[17] M.R. Cunha, E.C. Lima, D.R. Lima, R.S. da Silva, P.S. Thue, M.K. Seliem, F. Sher, G. S. dos Reis, S.H. Larsson, Removal of captopril pharmaceutical from synthetic pharmaceutical-industry wastewaters: use of activated carbon derived from Butia

catarinensis, J. Environ. Chem. Eng. 8 (2020), 104506, https://doi.org/10.1016/j.jece.2020.104506.
[18] L. Joseph, B.-M. Jun, M. Jang, C.M. Park, J.C. Muñoz-Senmache, A.J. Hernández-Maldonado, A. Heyden, M. Yu, Y. Yoon, Removal of contaminants of emerging concern by metal-organic framework nanoadsorbents: a review, Chem. Eng. J. 369 (2019) 928–946, https://doi.org/10.1016/j.cej.2019.03.173.
[19] S. Rojas, P. Horcajada, Metal-organic frameworks for the removal of emerging organic contaminants in water, Chem. Rev. 120 (2020) 8378–8415, https://doi.org/10.1021/acs.chemrev.9b00797.
[20] J.C. Munoz-Senmache, B. Fernandez-Reyes, A.J. Hernandez-Maldonado, Progress in the design of nanoporous adsorbent materials containing transition metals for the removal of contaminants of emerging concern, Environ. Pollut. Bioavaila. 33 (2021) 41–54, https://doi.org/10.1080/26395940.2021.1912643.
[21] Z. Zhang, H. Wang, X. Chen, C. Zhu, W. Wei, Y. Sun, Chromium-based metal–organic framework/mesoporous carbon composite: synthesis, characterization and CO_2 adsorption, Adsorption 21 (2015) 77–86, https://doi.org/10.1016/j10.1007/s10450-015-9651-2.
[22] J. Zhao, W.-W. Dong, Y.-P. Wu, Y.-N. Wang, C. Wang, D.-S. Li, Q.-C. Zhang, Two (3,6)-connected porous metal–organic frameworks based on linear trinuclear $[Co_3(COO)_6]$ and paddlewheel dinuclear $[Cu_2(COO)_4]$ SBUs: gas adsorption, photocatalytic behaviour, and magnetic properties, J. Mater. Chem. A 3 (2015) 6962–6969, https://doi.org/10.1016/j10.1039/C4TA06537A.
[23] J. Zhao, Y.-N. Wang, W.-W. Dong, Y.-P. Wu, D.-S. Li, Q.-C. Zhang, A robust luminescent Tb(III)-MOF with Lewis Basic pyridyl sites for the highly sensitive detection of metal ions and small molecules, Inorg. Chem. 55 (2016) 3265–3271, https://doi.org/10.1016/j10.1021/acs.inorgchem.5b02294.
[24] A. Dhakshinamoorthy, Z. Li, H. Garcia, Catalysis and photocatalysis by metal organic frameworks, Chem. Soc. Rev. 47 (2018) 8134–8172, https://doi.org/10.1039/C8CS00256H.
[25] Z.-S. Qin, W.-W. Dong, J. Zhao, Y.-P. Wu, Q. Zhang, D.-S. Li, A water-stable Tb(iii)-based metal–organic gel (MOG) for detection of antibiotics and explosives, Inorg. Chem. Front. 5 (2018) 120–126, https://doi.org/10.1016/j10.1039/C7QI00495H.
[26] A.Z. Aris, Z.A. Mohd Hir, M.R. Razak, Metal-organic frameworks (MOFs) for the adsorptive removal of selected endocrine disrupting compounds (EDCs) from aqueous solution: a review, Appl. Mater. Today 21 (2020), 100796, https://doi.org/10.1016/j.apmt.2020.100796.
[27] B.M. Connolly, D.G. Madden, A.E.H. Wheatley, D. Fairen-Jimenez, Shaping the future of fuel: Monolithic metal–organic frameworks for high-density gas storage, J. Am. Chem. Soc. 142 (2020) 8541–8549, https://doi.org/10.1021/jacs.0c00270.
[28] A. Rehman, S. Farrukh, A. Hussain, E. Pervaiz, Synthesis and effect of metal–organic frame works on CO_2 adsorption capacity at various pressures: a contemplating review, Energy Environ. 31 (2020) 367–388, https://doi.org/10.1016/j10.1177/0958305×19865352.
[29] Z.U. Zango, K. Jumbri, N.S. Sambudi, A. Ramli, N.H.H. Abu Bakar, B. Saad, M.N. H. Rozaini, H.A. Isiyaka, A.H. Jagaba, O. Aldaghri, A. Sulieman, A critical review on metal-organic frameworks and their composites as advanced materials for adsorption and photocatalytic degradation of emerging organic pollutants from wastewater, Polymers 12 (2020) 2648, https://doi.org/10.1016/j10.3390/polym12112648.
[30] A.J. Cruz, G. Arnauts, M. Obst, D.E. Kravchenko, P.M. Vereecken, S. De Feyter, I. Stassen, T. Hauffman, R. Ameloot, Effect of different oxide and hybrid precursors on MOF-CVD of ZIF-8 films, Dalton Trans. 50 (2021) 6784–6788, https://doi.org/10.1039/D1DT00927C.
[31] T. Stassin, R. Verbeke, A.J. Cruz, S. Rodríguez-Hermida, I. Stassen, J. Marreiros, M. Krishtab, M. Dickmann, W. Egger, I.F.J. Vankelecom, S. Furukawa, D. De Vos, D. Grosso, M. Thommes, R. Ameloot, Porosimetry for thin films of metal–organic frameworks: a comparison of positron annihilation lifetime spectroscopy and adsorption-based methods, Adv. Mater. 33 (2021) 2006993, https://doi.org/10.1002/adma.202006993.
[32] H. Wang, W. Ye, Y. Yang, Y. Zhong, Y. Hu, Zn-ion hybrid supercapacitors: achievements, challenges and future perspectives, Nano Energy 85 (2021), 105942, https://doi.org/10.1016/j.nanoen.2021.105942.
[33] I. Toumi, H. Djelad, F. Chouli, A. Benyoucef, Synthesis of PANI@ZnO hybrid material and evaluations in adsorption of congo red and methylene blue dyes: structural characterization and adsorption performance, J. Inorg. Organomet. Polym. Mater. 32 (2022) 112–121, https://doi.org/10.1016/j10.1007/s10904-021-02084-0.
[34] B. Liu, K. Vikrant, K.-H. Kim, V. Kumar, S.K. Kailasa, Critical role of water stability in metal–organic frameworks and advanced modification strategies for the extension of their applicability, Environ. Sci. Nano 7 (2020) 1319–1347, https://doi.org/10.1039/C9EN01321K.
[35] G. Férey, C. Serre, C. Mellot-Draznieks, F. Millange, S. Surblé, J. Dutour, I. Margiolaki, A hybrid solid with giant pores prepared by a combination of targeted chemistry, simulation, and powder diffraction, Angew. Chem. Int. Ed. 43 (2004) 6296–6301, https://doi.org/10.1002/anie.200460592.
[36] J.W. Yoon, H. Chang, S.-J. Lee, Y.K. Hwang, D.-Y. Hong, S.-K. Lee, J.S. Lee, S. Jang, T.-U. Yoon, K. Kwac, Y. Jung, R.S. Pillai, F. Faucher, A. Vimont, M. Daturi, G. Férey, C. Serre, G. Maurin, Y.-S. Bae, J.-S. Chang, Selective nitrogen capture by porous hybrid materials containing accessible transition metal ion sites, Nat. Mater. 16 (2017) 526–531, https://doi.org/10.1038/nmat4825.
[37] K.M. González-Ramos, B. Fernández-Reyes, F.R. Román, A.J. Hernández-Maldonado, A hierarchical porous carbon – M^{n+}[FAU] (M^{n+}=Ni^{2+} or Cu^{2+}) adsorbent: Synthesis, characterization and adsorption of salicylic acid from water, Microporous Mesoporous Mater. 200 (2014) 225–234, https://doi.org/10.1016/j.micromeso.2014.08.055.
[38] J.C. Muñoz-Senmache, S. Kim, R.R. Arrieta-Pérez, C.M. Park, Y. Yoon, A. J. Hernández-Maldonado, Activated carbon–metal organic framework composite for the adsorption of contaminants of emerging concern from water, ACS Appl. Nano Mater. 3 (2020) 2928–2940, https://doi.org/10.1021/acsanm.0c00190.
[39] B. Fernández-Reyes, S. Morales-Jiménez, J.C. Muñoz-Senmache, D.R. Vega-Santander, A.J. Hernández-Maldonado, Single- and multi-component adsorption of selected contaminants of emerging concern from water and some of their metabolites onto hierarchical porous copper(II)-zeolite -activated carbon composite, Microporous Mesoporous Mater. 312 (2021), 110355, https://doi.org/10.1016/j.micromeso.2020.110355.
[40] B. Fernández-Reyes, S. Morales-Jiménez, G. Sánchez-Marrero, J.C. Muñoz-Senmache, A.J. Hernández-Maldonado, Hierarchical three-dimensionally ordered mesoporous carbon (3DOm) zeolite composites for the adsorption of Contaminants of emerging concern, J. Hazard. Mater. Lett. 2 (2021), 100017, https://doi.org/10.1016/j.hazl.2021.100017.
[41] I. Ahmed, S.H. Jhung, Composites of metal–organic frameworks: preparation and application in adsorption, Mater. Today 17 (2014) 136–146, https://doi.org/10.1016/j.mattod.2014.03.002.
[42] M. Tong, D. Liu, Q. Yang, S. Devautour-Vinot, G. Maurin, C. Zhong, Influence of framework metal ions on the dye capture behavior of MIL-100 (Fe, Cr) MOF type solids, J. Mater. Chem. A 1 (2013) 8534–8537, https://doi.org/10.1039/C3TA11807J.
[43] G. Férey, C. Mellot-Draznieks, C. Serre, F. Millange, J. Dutour, S. Surblé, I. Margiolaki, A chromium terephthalate-based solid with unusually large pore volumes and surface area, Science 309 (2005) 2040–2042, https://doi.org/10.1126/science.1116275.
[44] M.F. De Lange, J.-J. Gutierrez-Sevillano, S. Hamad, T.J.H. Vlugt, S. Calero, J. Gascon, F. Kapteijn, Understanding adsorption of highly polar vapors on mesoporous MIL-100(Cr) and MIL-101(Cr): Experiments and molecular simulations, J. Phys. Chem. C 117 (2013) 7613–7622, https://doi.org/10.1021/jp3128077.
[45] S. Brunauer, P.H. Emmett, E. Teller, Adsorption of gases in multimolecular layers, J. Am. Chem. Soc. 60 (1938) 309–319, https://doi.org/10.1021/ja01269a023.
[46] E.P. Barrett, L.G. Joyner, P.P. Halenda, The determination of pore volume and area distributions in porous substances. I. Computations from nitrogen isotherms, J. Am. Chem. Soc. 73 (1951) 373–380, https://doi.org/10.1021/ja01145a126.
[47] S.U. Rege, R.T. Yang, Corrected Horváth-Kawazoe equations for pore-size distribution, AlChE J. 46 (2000) 734–750, https://doi.org/10.1002/aic.690460408.
[48] J. Crank, The Mathematics of Diffusion, Clarendon Press, Oxford, 1975.
[49] Y. Zhang, X. Bo, A. Nsabimana, C. Han, M. Li, L. Guo, Electrocatalytically active cobalt-based metal–organic framework with incorporated macroporous carbon composite for electrochemical applications, J. Mater. Chem. A 3 (2015) 732–738, https://doi.org/10.1039/C4TA04411H.
[50] P. Horcajada, S. Surblé, C. Serre, D.-Y. Hong, Y.-K. Seo, J.-S. Chang, J.-M. Grenèche, I. Margiolaki, G. Férey, Synthesis and catalytic properties of MIL-100 (Fe), an iron(III) carboxylate with large pores, Chem. Commun. (2007) 2820–2822, https://doi.org/10.1039/B704325B.
[51] S. Zhao, J. Mei, H. Xu, W. Liu, Z. Qu, Y. Cui, N. Yan, Research of mercury removal from sintering flue gas of iron and steel by the open metal site of Mil-101(Cr), J. Hazard. Mater. 351 (2018) 301–307, https://doi.org/10.1016/j.jhazmat.2017.12.016.
[52] D. Wang, Y. Ke, D. Guo, H. Guo, J. Chen, W. Weng, Facile fabrication of cauliflower-like MIL-100(Cr) and its simultaneous determination of Cd^{2+}, Pb^{2+}, Cu^{2+} and Hg^{2+} from aqueous solution, Sens. Actuators B Chem. 216 (2015) 504–510, https://doi.org/10.1016/j.snb.2015.04.054.
[53] S. Abdpour, E. Kowsari, M.R.A. Moghaddam, Synthesis of MIL-100(Fe)@MIL-53 (Fe) as a novel hybrid photocatalyst and evaluation photocatalytic and photoelectrochemical performance under visible light irradiation, J. Solid State Chem. 262 (2018) 172–180, https://doi.org/10.1016/j.jssc.2018.03.018.
[54] J.F. Moulder, W.F. Stickle, P.E. Sobol, K.D. Bomben, Handbook of X-ray Photoelectron Spectroscopy: A Reference Book of Standard Spectra for Identification and Interpretation of XPS data, Physical Electronics Division, Perkin-Elmer Corporation, 1992.
[55] S. Yao, J. Zhang, D. Shen, R. Xiao, S. Gu, M. Zhao, J. Liang, Removal of Pb(II) from water by the activated carbon modified by nitric acid under microwave heating, J. Colloid Interface Sci. 463 (2016) 118–127, https://doi.org/10.1016/j.jcis.2015.10.047.
[56] Q. Yang, P. Wu, J. Liu, S. Rehman, Z. Ahmed, B. Ruan, N. Zhu, Batch interaction of emerging tetracycline contaminant with novel phosphoric acid activated corn straw porous carbon: adsorption rate and nature of mechanism, Environ. Res. 181 (2020), 108899, https://doi.org/10.1016/j.envres.2019.108899.
[57] A. Behvandi, A.A. Safekordi, F. Khorasheh, Removal of benzoic acid from industrial wastewater using metal organic frameworks: equilibrium, kinetic and thermodynamic study, J. Porous Mater. 24 (2017) 165–178, https://doi.org/10.1007/s10934-016-0249-1.
[58] B. Nicolaï, B. Fournier, S. Dahaoui, J.-M. Gillet, N.-E. Ghermani, Crystal and electron properties of carbamazepine–aspirin co-crystal, Cryst. Growth Des. 19 (2019) 1308–1321, https://doi.org/10.1021/acs.cgd.8b01698.
[59] D.F. Caicedo, G.S. dos Reis, E.C. Lima, I.A.S. De Brum, P.S. Thue, B.G. Cazacliu, D. R. Lima, A.H. dos Santos, G.L. Dotto, Efficient adsorbent based on construction and demolition wastes functionalized with 3-aminopropyltriethoxysilane (APTES) for the removal ciprofloxacin from hospital synthetic effluents, J. Environ. Chem. Eng. 8 (2020), 103875, https://doi.org/10.1016/j.jece.2020.103875.
[60] J.J. Du, S.A. Stanton, S. Fakih, B.A. Hawkins, P.A. Williams, P.W. Groundwater, J. Overgaard, J.A. Platts, D.E. Hibbs, Exploring the solubility of the carbamazepine-

saccharin co-crystal: a charge density study, Cryst. Growth Des. 21 (2021) 259–4275, https://doi.org/10.1021/acs.cgd.8b01111.
[61] W. Qin, Z. Lin, H. Dong, X. Yuan, Z. Qiang, S. Liu, D. Xia, Kinetic and mechanistic insights into the abatement of clofibric acid by integrated UV/ozone/peroxydisulfate process: A modeling and theoretical study, Water Res. 186 (2020), 116336, https://doi.org/10.1016/j.watres.2020.116336.
[62] M. Uzzaman, M.J. Hoque, Physiochemical, molecular docking, and pharmacokinetic studies of Naproxen and its modified derivatives based on DFT, Int. J. Sci. Res. Manag. 6 (2018) 2018–2012–2019 (C-).
[63] S. Suresh, S. Gunasekaran, S. Srinivasan, Spectroscopic (FT-IR, FT-Raman, NMR and UV–Visible) and quantum chemical studies of molecular geometry, Frontier molecular orbital, NLO, NBO and thermodynamic properties of salicylic acid, Spectrochim. Acta Part A: Mol. Biomol. Spectrosc. 132 (2014) 130–141, https://doi.org/10.1016/j.saa.2014.04.174.
[64] S. Li, J. Wang, Y. Ye, Y. Tang, X. Li, F. Gu, L. Li, Composite Si-O-metal network catalysts with uneven electron distribution: enhanced activity and electron transfer for catalytic ozonation of carbamazepine, Appl. Catal. B 263 (2020), 118311, https://doi.org/10.1016/j.apcatb.2019.118311.
[65] H. Kaur, A. Bansiwal, G. Hippargi, G.R. Pophali, Effect of hydrophobicity of pharmaceuticals and personal care products for adsorption on activated carbon: adsorption isotherms, kinetics and mechanism, Environ. Sci. Pollut. Res. 25 (2018) 20473–20485, https://doi.org/10.1007/s11356-017-0054-7.
[66] M.A. Martín-González, O. González-Díaz, P. Susial, J. Araña, J.A. Herrera-Melián, J.M. Doña-Rodríguez, J. Pérez-Peña, Reuse of Phoenix canariensis palm frond mulch as biosorbent and as precursor of activated carbons for the adsorption of Imazalil in aqueous phase, Chem. Eng. J. 245 (2014) 348–358, https://doi.org/10.1016/j.cej.2014.02.050.
[67] L. Zhang, L.-y Tu, Y. Liang, Q. Chen, Z.-s Li, C.-h Li, Z.-h Wang, W. Li, Coconut-based activated carbon fibers for efficient adsorption of various organic dyes, RSC Adv. 8 (2018) 42280–42291, https://doi.org/10.1016/j10.1039/C8RA08990F.
[68] D.R. Lima, A. Hosseini-Bandegharaei, P.S. Thue, E.C. Lima, Y.R.T. de Albuquerque, G.S. dos Reis, C.S. Umpierres, S.L.P. Dias, H.N. Tran, Efficient acetaminophen removal from water and hospital effluents treatment by activated carbons derived from Brazil nutshells, Colloids Surf. A: Physicochem. Eng. Asp. 583 (2019), 123966, https://doi.org/10.1016/j.colsurfa.2019.123966.
[69] D.R. Lima, E.C. Lima, P.S. Thue, S.L.P. Dias, F.M. Machado, M.K. Seliem, F. Sher, G. S. dos Reis, M.R. Saeb, J. Rinklebe, Comparison of acidic leaching using a conventional and ultrasound-assisted method for preparation of magnetic-activated biochar, J. Environ. Chem. Eng. 9 (2021), 105865, https://doi.org/10.1016/j.jece.2021.105865.
[70] I. Anastopoulos, I. Pashalidis, A.G. Orfanos, I.D. Manariotis, T. Tatarchuk, L. Sellaoui, A. Bonilla-Petriciolet, A. Mittal, A. Núñez-Delgado, Removal of caffeine, nicotine and amoxicillin from (waste)waters by various adsorbents. A review, J. Environ. Manag. 261 (2020), 110236, https://doi.org/10.1016/j.jenvman.2020.110236.
[71] M. Francoeur, A. Ferino-Pérez, C. Yacou, C. Jean-Marius, E. Emmanuel, Y. Chérémond, U. Jauregui-Haza, S. Gaspard, Activated carbon synthetized from Sargassum (sp) for adsorption of caffeine: Understanding the adsorption mechanism using molecular modeling, J. Environ. Chem. Eng. 9 (2021), 104795, https://doi.org/10.1016/j.jece.2020.104795.
[72] J. Yang, B. Du, J. Liu, R. Krishna, F. Zhang, W. Zhou, Y. Wang, J. Li, B. Chen, MIL-100Cr with open Cr sites for a record N_2O capture, Chem. Commun. 54 (2018) 14061–14064, https://doi.org/10.1039/C8CC07679K.
[73] C. Chen, D. Chen, S. Xie, H. Quan, X. Luo, L. Guo, Adsorption behaviors of organic micropollutants on zirconium metal–organic framework UiO-66: analysis of surface interactions, ACS Appl. Mater. Interfaces 9 (2017) 41043–41054, https://doi.org/10.1021/acsami.7b13443.
[74] D. Chen, S. Wang, Z. Zhang, H. Quan, Y. Wang, Y. Jiang, M.J. Hurlock, Q. Zhang, Molten NaCl-induced MOF-derived carbon-polyhedron decorated carbon-nanosheet with high defects and high N-doping for boosting the removal of carbamazepine from water, Environ. Sci. Nano 7 (2020) 1205–1213, https://doi.org/10.1039/C9EN01408J.
[75] D. Chen, C. Chen, W. Shen, H. Quan, S. Chen, S. Xie, X. Luo, L. Guo, MOF-derived magnetic porous carbon-based sorbent: synthesis, characterization, and adsorption behavior of organic micropollutants, Adv. Powder Technol. 28 (2017) 1769–1779, https://doi.org/10.1016/j.apt.2017.04.018.